Mechanically-reconfigurable edge states in an ultrathin valley-hall topological metamaterial

Liu, Yahong; Ren, Huiling; Tao, Liyun; Du, Lianlian; Zhou, Xin; Li, Meize; Song, Kun; Ji, Ruonan; Zhao, Xiaopeng; Navarro-Cia, Miguel

License:
Other (please specify with Rights Statement)

Document Version
Peer reviewed version

[Link to publication on Research at Birmingham portal](#)

Mechanically-Reconfigurable Edge States in an Ultrathin Valley-Hall Topological Metamaterial

Yahong Liu[1*], Huiling Ren[1], Liyun Tao[1], Lianlian Du[1], Xin Zhou[2], Meize Li[1], Kun Song[1], Ruonan Ji[1], Xiaopeng Zhao[1], Miguel Navarro-Cía[3,4*]

[1]School of Physical Science and Technology, Northwestern Polytechnical University, Xi'an 710129, People's Republic of China.

[2]The National Research Institute of Radio Spectrum Management, Xi'an 710061, People's Republic of China.

[3]School of Physics and Astronomy, University of Birmingham, Birmingham B15 2TT, United Kingdom.

[4]Department of Electronic, Electrical and Systems Engineering, University of Birmingham, Birmingham B15 2TT, United Kingdom.

* Correspondence:

Yahong Liu

yhliu@nwpu.edu.cn

Miguel Navarro-Cía

m.navarro-cia@bham.ac.uk

Abstract

Broadband topological metamaterials hold the key for designing the next generation of integrated photonic platforms and microwave devices given their protected back-scattering-free and unidirectional edge states, among other exotic properties. However, synthesizing such metamaterial has proven challenging. Here, a broadband bandgap (relative bandwidth more than 43%) Valley-Hall topological metamaterial with deep subwavelength thickness is proposed. The present topological metamaterial is composed of three layers printed circuit boards (PCBs) whose total thickness is 1.524 mm $\sim \lambda/100$. The topological phase transition is achieved by introducing an asymmetry parameter δ_r. Three mechanically reconfigurable edge states can be obtained by varying interlayer displacement. We demonstrate their robust transmission through two kinds

of waveguide domain walls with cavities and disorders. Exploiting the proposed topological metamaterial, a six-way power divider is constructed and measured as a proof-of-concept of the potential of the proposed technology for future electromagnetic devices.

1 Introduction

Topological analogy of classical systems has attracted considerable attention in recent times for both fundamental science and engineering. In the science framework, several main mechanisms for the formation of topological edge states have been demonstrated including the construction of external magnetic field to achieve Quantum Hall effect (QHE) [1,2], the realization of Quantum Spin Hall effect (QSHE) based on band inversion [3-6], etc. In recent years, valley as a new degree of freedom has also been widely demonstrated. A pair of degenerates but not equivalent energy extreme in the momentum space, called valley [7-11], is one of the two high symmetry points (K and K') in the Brillouin zone. Since the definition is similar to electron spin, it can also be considered as pseudospin [12,13]. As the Dirac points in a valley system are no longer degenerate due to symmetry destruction, the bandgap may support the quantum Valley-Hall phase. So far, it has been demonstrated that the valley topological edge states can be obtained in the designer's surface plasmon polariton [7], sonic crystals [10,14,15], photonic crystals [3,16-22] and other systems by breaking the mirror symmetry or inversion symmetry. It is shown that the Valley-Hall system is exploited in many applications, such as topological channel intersections [12,21,23,24], optical switches [25-27], topological protected lasers [28-30], optical communication [31] and optoelectronic integration [32].

From an engineering perspective, deep subwavelength, broadband and electromagnetic robustness characteristics are critical for designing integrated photonic and microwave platforms. These properties are now actively pursued in the frame of topology. Chen *et al.* achieved two band gaps topological insulator by breaking inversion symmetry, with the thickness of 3.2 mm ($\lambda/2$) [33]. Wu *et al.* presented a surface plasmon polariton crystal with a thickness of 1.035 mm ($\lambda/38$) [7]. Kim *et al.*

proposed a dual-band photonic topological Valley-Hall edge states observed in square lattice [34], but the two bandgaps are narrow. Since degeneracy in the Valley-Hall system is lifted by breaking the mirror symmetry (rotation the unit cell) or breaking the spatial inversion symmetry (shrinking or expanding the size of unit cell) [10,15,16,19,33], the bandgap is limited by its geometric shape, resulting in narrow bandgaps. By changing the structures from a staggered honeycomb to a hexagonal lattice, a larger bandgap has been studied [40,41]. Recently, reconfigurable topological edge state [35,36] provides the possibility of achieving a multi-band or broadband transmission [25,26,37,38]. Gao *et al.* [27] proposed a tunable phononic crystal plate composed of a *Y*-shaped prism to support the valley transport of elastic waves, and realized the reconfigurable waveguide structure by rotating the prism. Wu *et al.* achieved reconfiguration by adjusting the refractive index of the dielectric rods [25]. In addition, there are also some schemes to realize reconfiguration by applying external conditions, such as controlling computer motorized stage to modify the shape of domain wall [26], altering the same parameter for all posts [37], and introducing external electric field to change the refractive index of liquid crystals [38], etc.

Although Valley-Hall topological materials have made great progress, most topological insulators especially topological crystals have the characteristics of large volume, narrow bandgap, and single-band topological edge state. Therefore, designing an ultrathin, broadband, reconfigurable topological metamaterial is still a challenge. In this paper, we propose a Valley-Hall topological metamaterial consisting of three layers of PCBs, with a thickness of 1.524 mm (about $\lambda/100$). The lifting of degeneracy is generated by introducing asymmetry parameter δ_r, resulting in a topological bandgap with a relative bandwidth of 43%. The proposed bandwidth exceeds the previously demonstrated topological bandgap widths of 12% in two-dimensional scheme [7, 26], and 25% bandgap widths in the recently proposed three-dimensional spin-Hall topological insulator [39]. Reconfigurable topological edge states can be realized by varying interlayer displacement, which achieves frequency tunability over a wide frequency range. In addition, we construct two-dimensional waveguides by using the present reconfigurable topological edge states, and demonstrate the robust transmission

against defects. Finally, a six-way power divider based on the proposed topological metamaterial is demonstrated. Due to the advantages of extremely broad bandgap, reconfiguration of the edge states, and the high integration by using circuit board etching technology, the proposed Valley-Hall topological metamaterial hold promise for the next generation of integrated photonic and microwave circuits.

2 Design of a Valley-Hall topological metamaterial

2.1 Theoretical model and band structure

Figure 1(a) depicts the proposed structure consisting of three layers. Each layer is deposited 0.035 mm thickness copper patterns in a F4B substrate with a thickness of h_1 = 0.508mm, a relative dielectric constant of 4.4 and a loss tangent of 0.0025. In the first layer, circular copper patches with a radius of $R_1 = R_2$ are arranged in a hexagonal tiling on one side of a dielectric substrate. The distance between the center of the two circular patches is R. The second layer is a snowflake copper patterns deposited on the one side of a dielectric substrate. The snowflake copper patterns are connected by hexagons with the side length l_1. The copper wires length and width are l_2 and l_3, respectively. The third layer is the same as the first one. The unit cell is shown in the upper inset of Figure 1(a). The lattice constant is a = 16 mm, p (red dot) and q (blue dot) are the centers of two non-equivalent triangular lattices. For visualization purposes, the copper thickness in Figure 1(a) is exaggerated and three-layer substrates are separated by h_2 (the actual height h_2 is 0 mm). The total thickness of the present structure is $h = 3h_1$ = 1.524 mm. The fabricated sample with three-layer structure is shown in Figure 1(b).

Numerical simulations and experiments were carried out to study the electromagnetic properties of the present Valley-Hall topological metamaterials. The simulations were obtained by using the commercial software Ansys HFSS. Figure 1(c) presents the band diagram of a unit cell, which shows a Dirac cone is observed with a frequency of 1.976 GHz at the K (K'). Figure 1(d) displays two degeneracy states of valley K, corresponding to right-hand circularly polarization (RCP) and left-hand circularly

polarization (LCP), respectively. The color depicts the amplitudes of the out-of-plane electric field component and the green arrows represent the energy fluxes.

The experiments were carried out in an anechoic chamber composed of an AV 3629 vector network analyzer (45 MHz ~ 40 GHz) and two monopole antennas. As shown in **Figure 2**, one monopole antenna acts as a source connected to the port 1 of the vector network analyzer, and other monopole antenna acts as a detector connected to the port 2 of the vector network analyzer. Both monopole antennas are placed on each side of the sample to measure transmission spectrum.
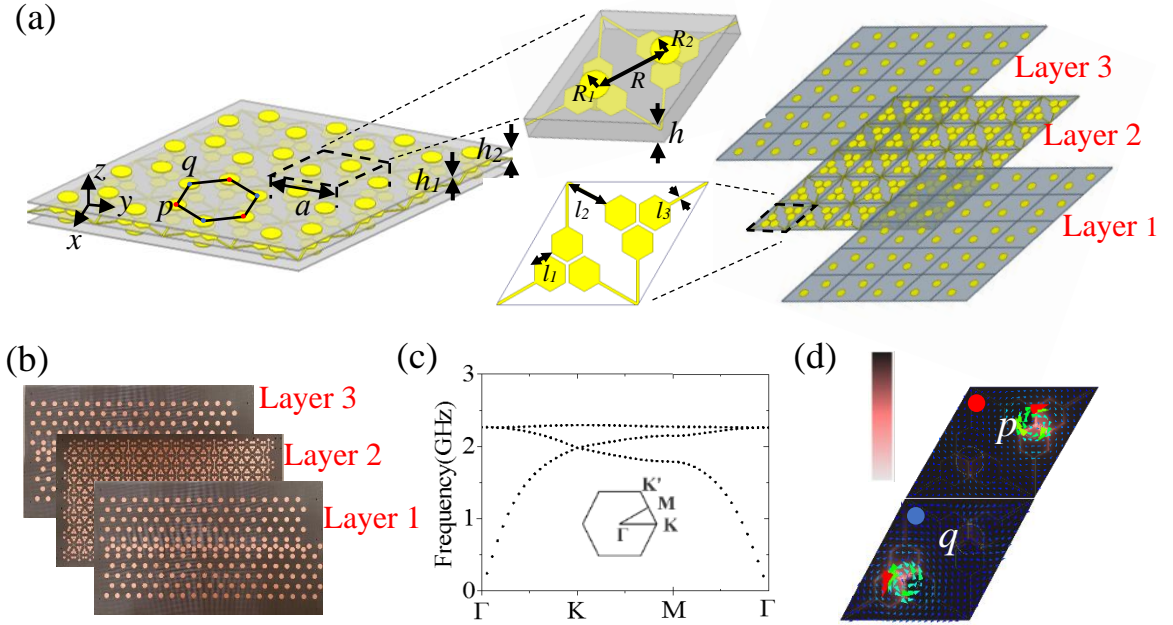
Figure 1. (a) Schematic view of the proposed Valley-Hall photonic topological metamaterial. Geometry parameters are shown as: $l_1 = 2$ mm, $l_2 = 7$ mm, $l_3 = 0.3$ mm, $R = 16/\sqrt{3}$ mm, $R_1 = R_2 = 1.75$ mm, $h_1 = 0.508$ mm, $h_2 = 0$ mm, $h = 3h_1 = 1.524$ mm, and $a = 16$ mm. Yellow color indicates copper and gray color indicates F4B substrate. (b) Fabricated sample with three-layer structure. (c) Band structure of the proposed metamaterial with $R_1 = R_2 = 1.75$ mm, and the inset is the first Brillouin zone. (d) Electric field distributions and Poynting vectors at the K valley.

Figure 2. Experimental setup for the transmission measurement.

2.2 Asymmetric structures and topological phase transition

We design three topological structures that can generate Dirac cones at different frequencies. As shown in **Figure 3**(a), varying the radius of circular patches from $R_1 = R_2 = 1.75$ mm (Figure 1(c)) to $R_1 = R_2 = 3.5$ mm, leads to a frequency shift of the Dirac point from 1.976 GHz to 1.49 GHz. The larger the radius of the circular patches is, the lower the frequency of Dirac point is. If we modify the structure corresponding to Figure 3(a) by changing R_2 of the first layer from 1.75 mm to 0 mm, and R_1 of the third layer from 1.75 mm to 0 mm, the frequency of the Dirac point moves to 1.78 GHz (see Figure 3(b)). Finally, if we change the lattice symmetry from C_6 (Figure 3(a, b)) to C_{3v} (Figure 3(c)) by displacing the center of the circular patch to the lattice point, the Dirac point frequency is further shifted to 2.6 GHz. The results show that the frequency of the Dirac cones can be varied by the configurations and the geometrical parameters.
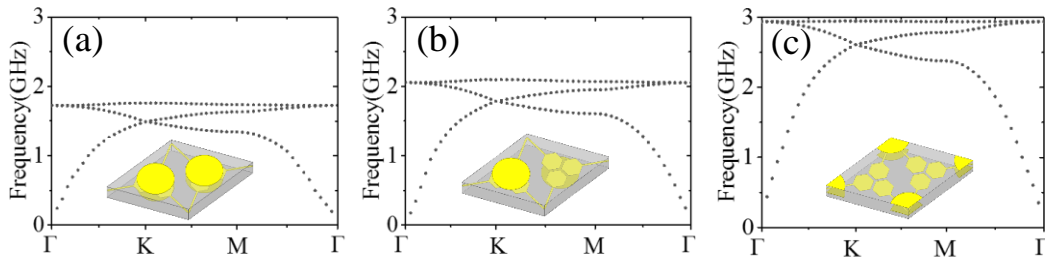

Figure 3. (a) Band structure for the unit cell with $R_1 = R_2 = 3.5$ mm. (b) Band structure for the unit cell where R_2 of the first layer is changed to 0 mm and R_1 of the third layer is changed to 0 mm. (c) Band structure for the unit cell as the circular patches shown in Figure 3(a) are moved to the lattice point.

We introduce asymmetry parameter $\delta_r = R_1 - R_2$. Degeneracy is lifted by changing δ_r, resulting in a complete broadband gap covered from 1.476 GHz to 2.355 GHz, as shown in **Figure 4**(b). The unit cells of $\delta_r = R_1 - R_2 = -3.5$ mm and $\delta_r = R_1 - R_2 = 3.5$ mm are shown in Figures 4(a) and 4(c), respectively. As $R_1 = 0$ mm or $R_2 = 0$ mm, the symmetry of hexagonal lattice is reduced to C_3 as compared to the structure with $R_1 = R_2 \neq 0$ (C_6). The structures shown in Figure 4(a) and Figure 4(c) have the same band structure as presented in Figure 4(b), showing a broadband gap with a relative bandwidth over 43%.

Indeed, this asymmetrical structure can be obtained simply by moving the interlayer displacement. As shown in Figure 4(a), the metallic circular patches of the first and third layers are $R_1 = 0$ mm and $R_2 = 3.5$ mm, and those of the first and third layers in Figure 4(c) are $R_1 = 3.5$ mm and $R_2 = 0$ mm. Figure 4(a) can be transformed into Figure 4(c) by simultaneously moving the layer 1 and layer 3 the distance of R, while the layer 2 is fixed. The corresponding electric component and energy fluxes of Figures 4(a) and 4(c) at the K and K' for the first and second bands are shown in Figure 4(d). As $\delta_r = -3.5$ mm, the direction of its energy fluxes at the K and K' for the first band shows RCP and LCP, respectively. For the second band, the energy flux shows LCP and RCP at the K and K', respectively. However, as $\delta_r = 3.5$ mm, the direction of energy fluxes are LCP and RCP at the K and K' for the first band, and the second band are RCP and LCP at the K and K'. Figure 4(d) shows that the direction of energy fluxes of Figure 4(a) in the second band is the same as those of Figure 4(c) in the first band, whereas the direction of energy fluxes of Figure 4(a) in the first band is the same as those of Figure 4(c) in the second band. The results indicate that a phase transition occurs.
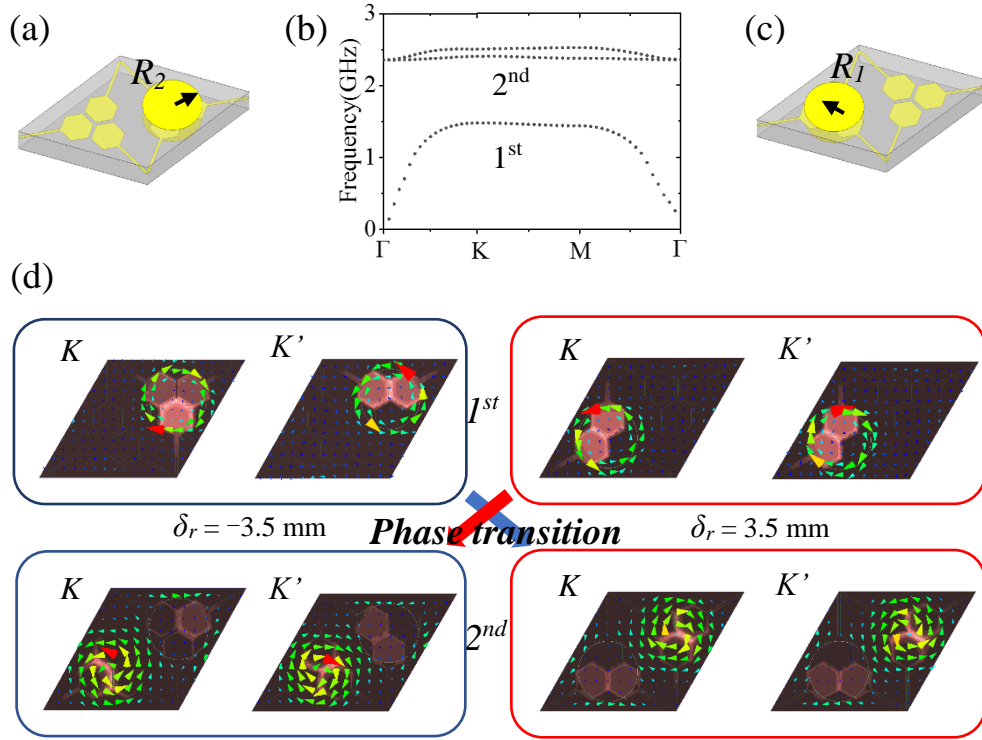
Figure 4. Unit cell with (a) $\delta_r = R_1 - R_2 = -3.5$ mm and (c) $\delta_r = R_1 - R_2 = 3.5$ mm. (b) Band structure for the configurations of Figures 4(a) and 4(c). (d) Electric field and Poynting vector distributions at the K and K' for the first and second bands. As δ_r varies from -3.5 mm to 3.5 mm, the topological phase transition occurs.

2.3 Berry curvature and Valley Chern number

The phase diagram in **Figure 5**(a) displays the variation of frequency as a function of δ_r at the K and K', while keeping $R_1 + R_2 = 3.5$ mm. As $\delta_r > 0$ mm, R_1 gradually increases from 1.75 mm to 3.5 mm, and R_2 gradually decreases from 1.75 mm to 0 mm. When $\delta_r < 0$ mm, R_1 gradually decreases from 1.75 mm to 0 mm, and R_2 gradually increases from 1.75 mm to 3.5 mm. We chose 19 points with various δ_r and observed the direction of energy fluxes of 1st band and 2nd band. In the region of $\delta_r < 0$ mm, the K valley frequency of the RCP gradually increases as δ_r increases from -3.5 to 0 mm, while the K valley frequency of the LCP and the K' valley frequency of the RCP gradually decrease. In the region of $\delta_r > 0$, the K valley frequency of the RCP gradually increases as δ_r increases from 0 to 3.5 mm, while the K valley frequency of the LCP and the K' valley frequency of the RCP gradually decrease. As $\delta_r = 0$, 1st band and 2nd band cross, indicating topological phase transition.

We perform numerical simulations in Ansys HFSS to calculate the Berry curvature of the 2nd band near the K valley and K' valley for the unit cell with $\delta r = R_1 - R_2 = -3.5$ mm. The calculation of Valley Chern number is based on the finite element method, which simplifies the hexagonal Brillouin region of the structure. We choose the rhomboid Brillouin region containing K valley and K' Valley, and divides it into uniform quadrilateral small regions, $\delta_{kx} = \frac{2\pi}{3}(x+y)$, $\delta_{ky} = \frac{2\pi\sqrt{3}}{3}(x-y)$, where $x=[0, ..., 2\pi]$, and $y=[0, ..., 2\pi]$. The Berry curvature diagram obtained by finite element calculation is shown in Figure 5(b). Note that the Berry curvatures near the K' valley are opposite to those near the K valley. Integrating the Berry curvatures near the K valley and K' valley, we can obtain the valley Chern number at the K/K' valley. Valley Chern number can be expressed as $C = (C_K - C_{K'})$, where $C_{K/K'} = \pm \text{sgn}(\delta_r)/2$. The absolute value of the valley Chern number near the K valley and the K' valley is smaller than 1/2 due to the large bandgap for the proposed structure. According to the sign of the valley Chern number, as long as the states of the K valley and K' valley are orthogonal to each other, the valley Chern number will guarantee topological protection to the Valley-Hall phase [19].
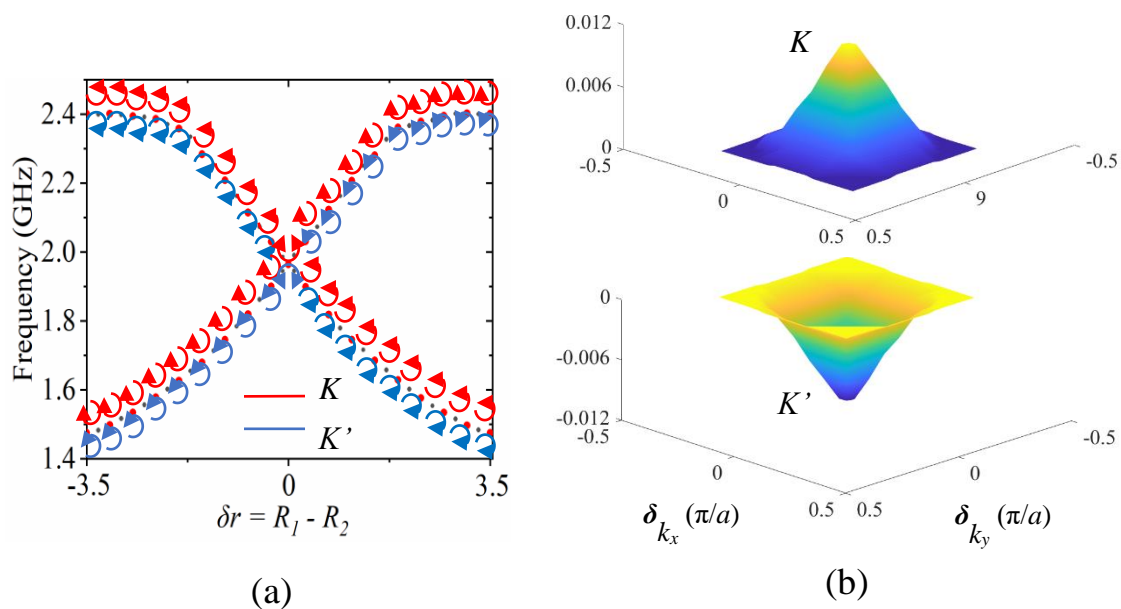

Figure 5. (a) Variation of frequency with δ_r ($\delta_r = 0$ corresponds to $R_1 = R_2 = 1.75$ mm). The K and K' are represented by red and blue circular arrows, respectively. The 19 points are represented by red dots with various $\delta_r = -3.5$ mm, -3.1 mm, -2.7 mm, -2.3 mm, -1.9 mm, -1.5

mm, -1.1 mm, -0.7 mm, -0.3 mm, 0 mm, 0.3 mm, 0.7 mm, 1.1 mm, 1.5 mm, 1.9 mm, 2.3 mm, 2.7 mm, 3.1 mm, and 3.5 mm. (b) Numerically calculated Berry curvature of the 2nd band at the K valley and the K' valley.

3 Reconfigurable topological edge states

By varying the interlayer displacement of the three PCB layers, three types of interfaces can be mechanically reconfigured by using a supercell consisting of two configurations with distinct topological index: $\delta_r = -3.5$ mm and $\delta_r = 3.5$ mm. **Figure 6**(a) presents the interface I, where $\delta_r = -3.5$ mm is on the bottom and $\delta_r = 3.5$ mm is on the top. The unit cell at the interface is indicated by a red dashed diamond. The black dotted curves in the dispersion represent the projection of bulk band, and the topological edge state is shown in red solid line. The frequency of 1.62 GHz at the $k_x = \pi/2a$ on the edge state line is chosen. The corresponding electric field distribution and direction of energy fluxes show the electric field energy is highly localized around the interface I. However, besides the topological edge state, it is notable that there are two redundant bands as shown in black solid lines. In order to explore the underlying physics of the redundant two bands, we calculate the dispersion relationship of each half structure as shown in the bottom panel in Figure 6(a). The dispersion relationship shows the two black solid lines still exist even if no interface is formed. We also calculate the electric field distributions at the frequencies of 1.66 GHz and 1.73 GHz at the $k_x = \pi/2a$ on these two redundant bands, which demonstrates field localization. Actually, a new unit cell is introduced at the interface I due to the reconfigurability, which the degeneracy point cannot be opened and then electromagnetic waves can transmit. Therefore, these two bands are the inherent property of the introduced new structure, and they are trivial bands but not the topological edge states. Based on the analysis above, only the one edge state shown in red solid line is the topological edge state of the interface I.

Based on the interface I, we construct the interface II by moving interlayer displacement as shown in Figure 6(b). By moving the supercells of the first layer one lattice constant along the direction of the blue arrow, and moving the supercells of the first layer one lattice constant along the direction of the black arrow, the new configuration (the interface II) can be obtained. The corresponding dispersion is similar

to that of the interface I where the red solid line is the topological edge state. We investigated the electric field distributions and direction of energy fluxes at 1.77 GHz, which shows that energy is localized at the expected interface. The two black solid lines are not the topological edge state, which are also due to the inherent property of the structure.
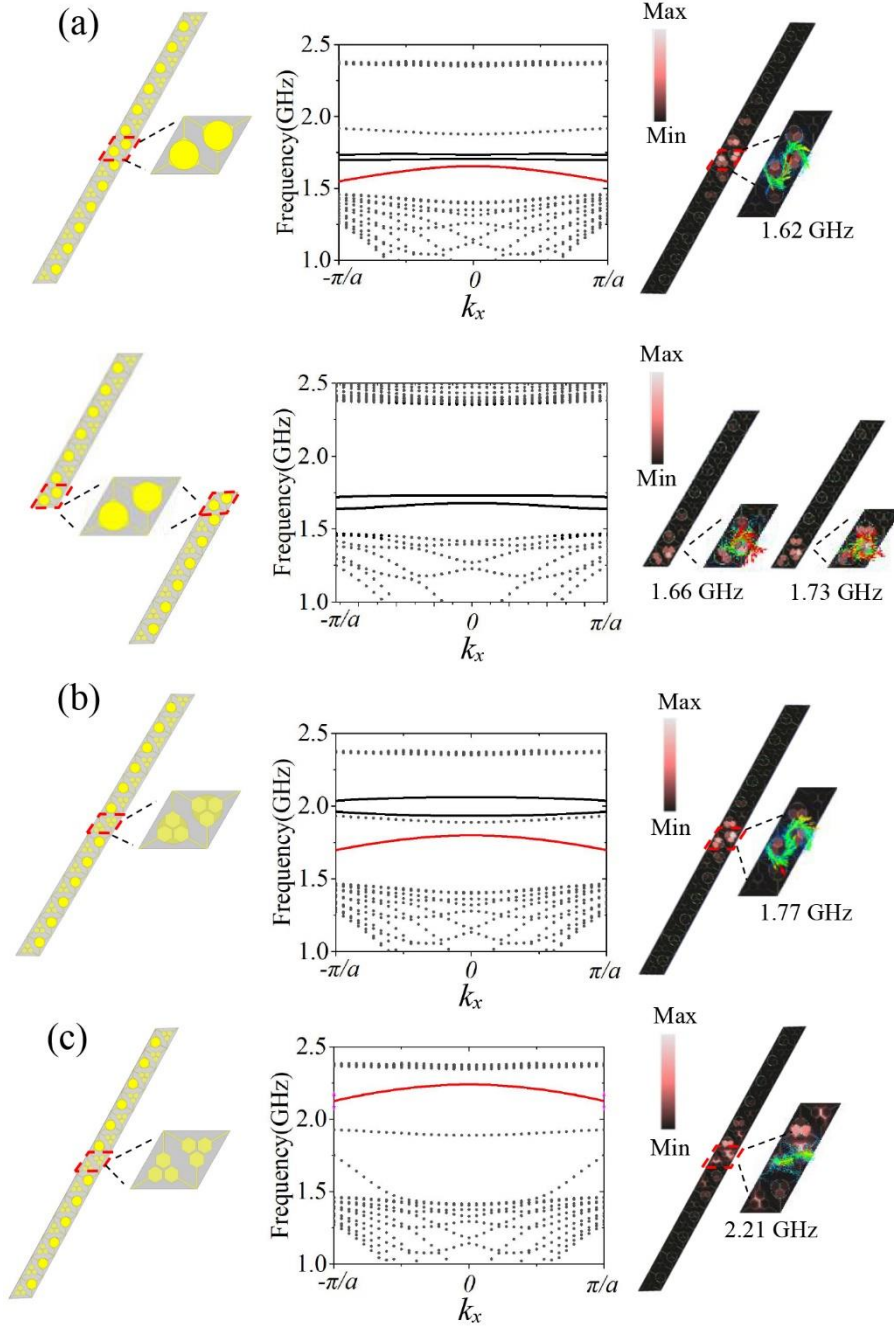

Figure 6. Different topological edge states can be reconfigured by using two topologically distinct unit cells. The unit cell at the interface is labeled by a red dashed diamond. Topological supercell, dispersion, and electric field distributions for the (a) interface I, (b) interface II, and (c) interface III.

The black dotted curves and red solid lines represent the projection of bulk bands and edge states, respectively. The bottom panel in Figure 6(a) is the dispersion relationship of each half structure, which has two trivial bands shown in black solid lines.

On the basis of the interface II, interface III can be obtained by moving the third layer in the same way as shown in Figure 6(b). Different from the band structure of the interfaces I and II, the dispersion show that the interface III has one topological edge state. No redundant boundary state is observed. This is due to the fact that the interface III does not introduce any new structure. The formed supercell has one lattice constant gap that makes frequency of the edge state to blue shift. The electric field component and Poynting vector distribution of 2.21 GHz at $k_x = \pi/2a$ are presented in Figure 6(c). The above results show that the different topological edge states are obtained by different reconfigurable interfaces.

In addition, it is notable that the dispersion curves of the three interfaces in Figure 6 shows there is a black dotted line around 1.9 GHz. It is caused by the long period approximation. As $k_x = \pi/2a$ is selected from the long period approximate line in Figure 6(a), the corresponding electric field intensity distribution is shown in **Figure 7**(a). It can be seen that the energy is localized at the ends of the supercell not the interface. The similar results are obtained for the interfaces II and III as shown in Figures 7(b) and 7(c), respectively.

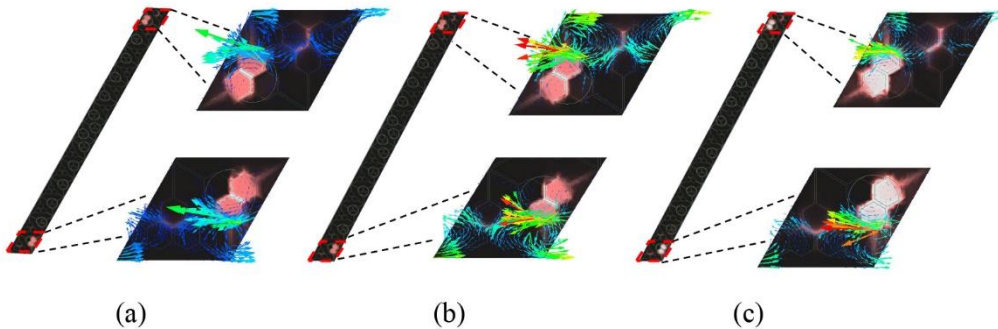(a)   (b)   (c)

Figure 7. Electric field distributions and energy flux directions of the long period approximate line at $k_x = \pi/2a$ for the (a) interface I, (b) interface II, and (c) interface III.

4 Reconfigurable waveguides

Based on the preliminary studies shown so far, since three different topological interfaces can be found by varying interlayer displacement, we can construct three different reconfigurable Valley-Hall topological metamaterial waveguides. Two kinds of the fabricated samples (reconfigurable straight waveguides and reconfigurable bent waveguides) are shown in **Figures** 8(a) and 8(b), respectively. For each waveguide, three interfaces can also be reconfigured.

As displayed in Figure 8(a), the reconfigurable straight waveguide consists of three-layered structure with five pieces of PCBs indicated by 1, 2, 3, 4 and 5. Piece 1 and piece 2 form layer 1. Piece 3 and piece 4 form layer 3. That is to say, the layer 1 and layer 3 are both zigzag split down the middle into two pieces. The whole piece 5 acts as layer 2. When the two pieces of the layer 1 and the two pieces of the layer 3 are tightly packed together without gap, and layer 2 is sandwiched by the layer 1 and layer 3, a straight domain wall is constructed as shown in Figure 8(c). The interface of this domain wall is the same of the interface I as shown in Figure 6(a). We refer to the domain wall as the straight waveguide I in the following sections. If we move the two pieces of the layer 1 with a gap of one lattice constant, and the other two layers are fixed, then the reconfigurable straight waveguide II is achieved as presented in Figure 8(e). The interface of this domain wall is the same as the interface II as shown in Figure 6(b). If the two pieces of layer 1 and the two pieces of layer 3 are both moved with a gap of one lattice constant, the straight waveguide III is formed, as shown in Figure 8(g). Therefore, five pieces PCBs can achieve three different straight waveguides.

Using the same method of the reconfigurable straight waveguide, a reconfigurable bent waveguide can also be constructed as shown in Figure 8(b). The bent waveguide is composed of seven pieces of PCBs. The reconfigurable bent waveguides I, II and III are presented in Figures 8(d), 8(f) and 8(h).
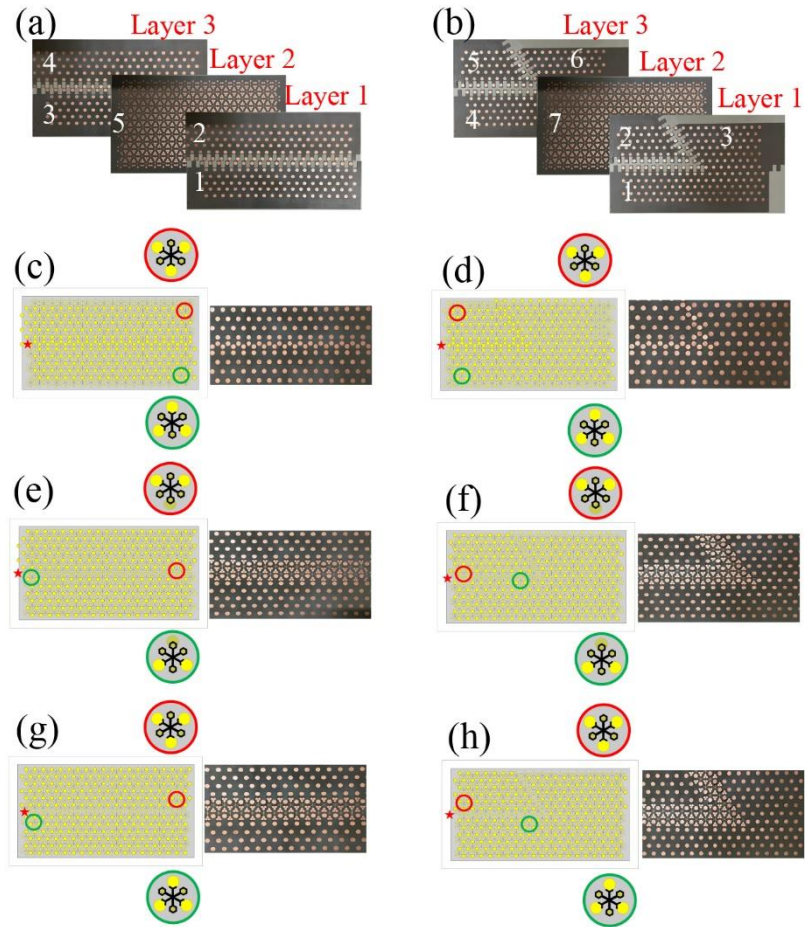
Figure 8. Fabricated samples of (a) the reconfigurable straight waveguide and (b) reconfigurable bent waveguide. Three interfaces can be reconfigured by moving each layer. Schematic top view and the fabricated samples of (c) straight and (d) bent waveguide I. Schematic top view and the fabricated samples of (e) straight and (f) bent waveguide II. Schematic top view and the fabricated samples of (g) straight and (h) bent waveguide III.

Simulated electric field intensity distributions and the measured transmission spectrums for the straight and bent waveguides are presented in **Figure 9**, which shows robust high transmissions in both domains. The measured transmission spectrums agree with simulations. All the above waveguides can achieve high transmission. The slight deviation between the simulation and experimental results is due to the inhomogeneous dielectric constant and the spacings between multilayer dielectric plates.
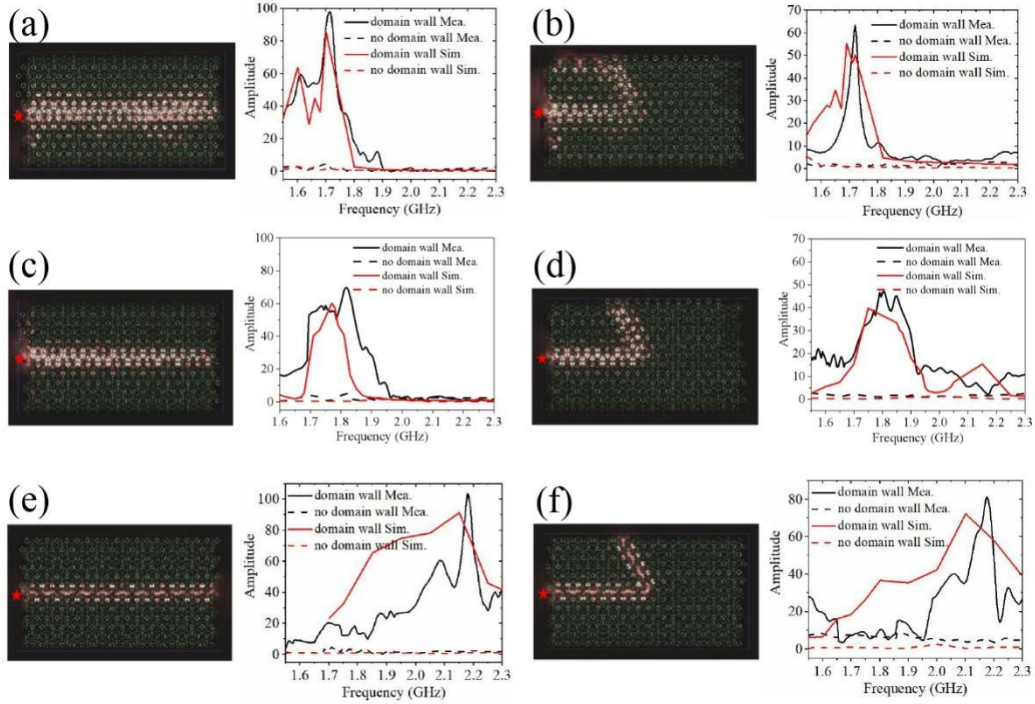
Figure 9. Simulated electric field intensity distributions and measured transmission of the (a) straight and (b) bent topological metamaterial waveguide I. Simulated electric field intensity distributions and measured transmission of the (c) straight and (d) bent topological metamaterial waveguide II. Simulated electric field intensity distributions and measured transmission of the (e) straight and (f) bent topological metamaterial waveguide III. The red star indicates the excitation source.

To further demonstrate the robustness of the waveguide transmission, two defects (cavity and disorder) are introduced in the waveguides. We investigated the robust transmission of the waveguide II, as an example. Cavity defect can be constructed by removing the unit cells at the red dashed circles, and the disorder defect can be obtained by moving the position of circular patches from the dashed blue line to the solid blue line. **Figures 10**(a) and 10(b) are the simulated electric field intensity distribution of the straight domain wall with cavity and disorder defects, respectively. The results show electromagnetic wave can propagate smoothly along the straight domain walls, and the transmission is immune to either cavity or disorder. The compared transmission spectrums between the defects and no defects of the straight waveguide are shown in Figure 10(e).

Next, we introduce cavity defect and disorder defect into the bent domain wall, as presented in Figures. 10(c) and 10(d), respectively. The field distributions show the backscattering can be negligible. Even if there is a disorder or a cavity, smooth wave propagation still exists along the interface. These results confirm the robust transmission of the designed waveguide. The compared transmission spectrums between the defects and no defects of the bent waveguide are presented in Figure 10(f).
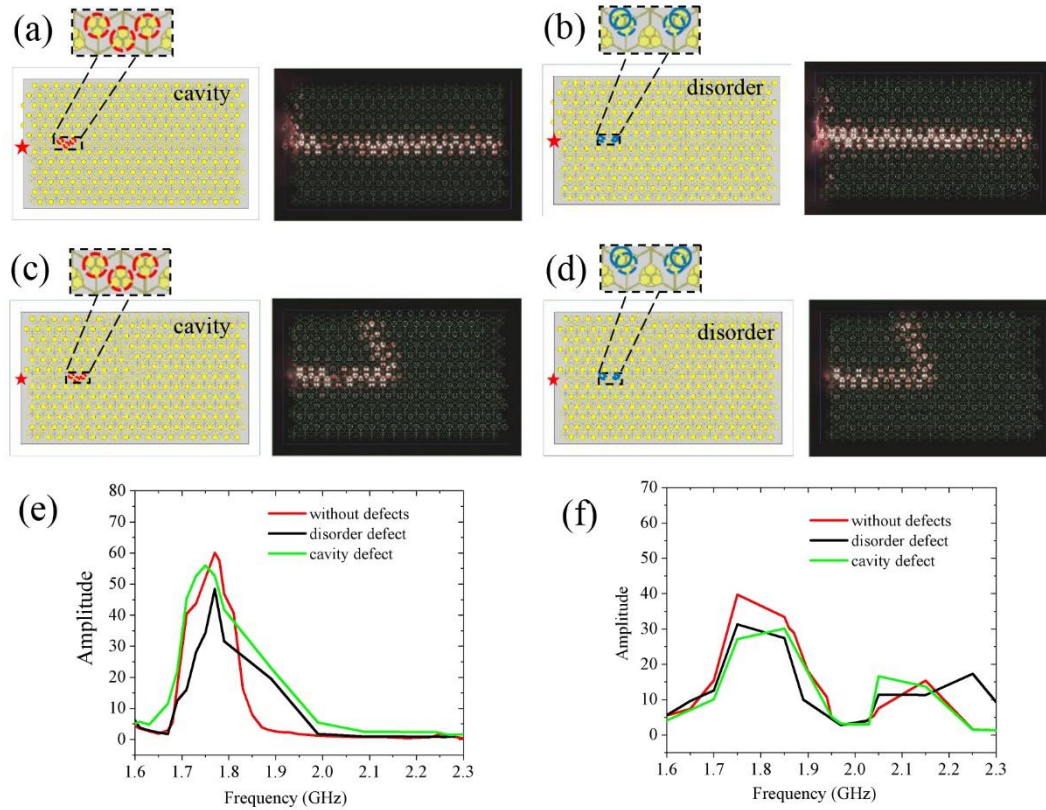

Figure 10. Schematic view and simulated field intensity distributions of (a) cavity defect and (b) disorder defect of the straight waveguide. Schematic view and simulated field intensity distributions of (c) cavity defect and (d) disorder defect of the bent waveguide. The red star indicates the excitation source. Compared transmission between the defects and no defects of (e) the straight waveguide and (f) the bent waveguide.

5 Power divider

Finally, we design a six-way power divider shown in **Figure 11** as a further proof-of-concept of the potential of the proposed topological metamaterial for circuitry. Here, we constructure the channel interface by using the supercells. The present six-way

power divider consisting of the supercells A and B. Due to the particularity of the proposed structure, the interfaces of the six domain walls of the structure are the exact same, and they are both the interface I by means of mechanical reconstruction. The excitation source indicated as a red star is placed at the bottom of the Figure 11(a). The distribution of the electric field intensity of the six-channel power divider shows that electromagnetic wave can transmit along the expected six channels. The measured transmission spectrums are in agreement with the simulated electric field distribution. However, in previously published literatures [7,42], there was a clear distinction between the structures above and below the domain walls, showing valley selectivity.
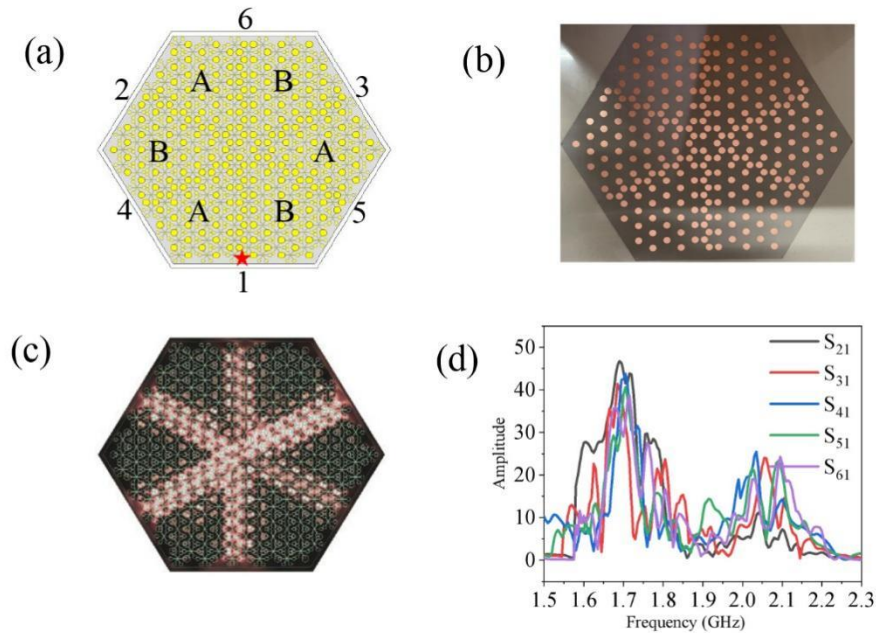

Figure 11. (a) Schematic view of the six-way power divider, (b) top view of the fabricated sample, (c) simulated electric field intensity distribution at 1.62 GHz, and (d) measured transmission spectrum of the six-way power divider. Six wave paths are labeled by 1-6.

6 Conclusions

In conclusion, we propose reconfigurable edge states in Valley-Hall topological metamaterial consisting of the two configurations with distinct topological index. Three different reconfigurable topological edge states can be observed by simply varying interlayer displacement. We construct straight waveguides and bent waveguides by using the present reconfigurable topological edge states. It is demonstrated that electromagnetic wave can be transmitted without scattering along the waveguides.

Moreover, the transmission is robust and immune to the cavities or disorders. Finally, we construct a six-way power divider. Our proposed structure has the advantages of wide band gap, ultra-thin thickness, immune to defects, and good compatibility with printed circuit board technology. It has potential applications in unidirectional waveguides, integrated photonic circuits, topological signal processing and so on.

References

[1] M. Hafezi, E. A. Demler, M. D. Lukin, J. M. Taylor, *Nature Phys.* **2011**, *7*, 907.

[2] Z. Wang, Y. Chong, J. D. Joannopoulos, M. Soljačić, *Nature* **2009**, *461*, 772.

[3] J.-W. Dong, X.-D. Chen, H. Zhu, Y. Wang, X. Zhang, *Nature Mater*. **2017**, *16*, 298.

[4] S. Barik, H. Miyake, W. DeGottardi, E. Waks, M. Hafezi, *New J. Phys*. **2016**, *18*, 113013.

[5] L.-H. Wu, X. Hu, *Phys. Rev. Lett.* **2015**, *114*, 223901.

[6] Y. Wang, Y. Dong, S. Zhai, C. Ding, C. Luo, X. Zhao, *Phys. Rev. B* **2020**, *102*, 174107.

[7] X. Wu, Y. Meng, J. Tian, Y. Huang, H. Xiang, D. Han, W. Wen, *Nat. Commun.* **2017**, *8*, 1304.

[8] G.-J. Tang, X.-D. Chen, F.-L. Shi, J.-W. Liu, M. Chen, J.-W. Dong, *Phys. Rev. B* **2020**, *102*, 174202.

[9] M. Kim, Z. Jacob, J. Rho, *Light Sci. Appl.* **2020**, *9*, 130.

[10] J. Lu, C. Qiu, L. Ye, X. Fan, M. Ke, F. Zhang, Z. Liu, *Nature Phys.* **2017**, *13*, 369.

[11] L. Ye, Y. Yang, Z. Hong Hang, C. Qiu, Z. Liu, *Appl. Phys. Lett.* **2017**, *111*, 251107.

[12] Y. Kang, X. Ni, X. Cheng, A. B. Khanikaev, A. Z. Genack, *Nat. Commun.* **2018**, *9*,

3029.

[13] S. Huo, J. Chen, L. Feng, H. Huang, *J. Acoust. Soc. Am.* **2019**, *146*, 729.

[14] Y. Yang, Z. Yang, B. Zhang, *J. Appl. Phys.* **2018**, *123*, 091713.

[15] J. Lu, C. Qiu, W. Deng, X. Huang, F. Li, F. Zhang, S. Chen, Z. Liu, *Phys. Rev. Lett.* **2018**, *120*, 116802.

[16] M. I. Shalaev, W. Walasik, A. Tsukernik, Y. Xu, N. M. Litchinitser, *Nature Nanotech.* **2019**, *14*, 31.

[17] F. Gao, H. Xue, Z. Yang, K. Lai, Y. Yu, X. Lin, Y. Chong, G. Shvets, B. Zhang, *Nat. Phys.* **2018**, *14*, 140.

[18] J. Noh, S. Huang, K. P. Chen, M. C. Rechtsman, *Phys. Rev. Lett.* **2018**, *120*, 063902.

[19] X.-T. He, E.-T. Liang, J.-J. Yuan, H.-Y. Qiu, X.-D. Chen, F.-L. Zhao, J.-W. Dong, *Nat. Commun.* **2019**, *10*, 872.

[20] Z. Gao, Z. Yang, F. Gao, H. Xue, Y. Yang, J. Dong, B. Zhang, *Phys. Rev. B* **2017**, *96*, 201402.

[21] L. Zhang, Y. Yang, M. He, H. Wang, Z. Yang, E. Li, F. Gao, B. Zhang, R. Singh, J. Jiang, H. Chen, *Laser Photonics Rev.* **2019**, *13*, 1900159.

[22] T. Ma, G. Shvets, *New J. Phys.* **2016**, *18*, 025012.

[23] G.-C. Wei, Z.-Z. Liu, D.-S. Zhang, J.-J. Xiao, *New J. Phys.* **2021**, *23*, 023029.

[24] Z. Qiao, J. Jung, C. Lin, Y. Ren, A. H. MacDonald, Q. Niu, *Phys. Rev. Lett.* **2014**, *112*, 206601.

[25] Y. Wu, X. Hu, Q. Gong, *Phys. Rev. Materials* **2018**, *2*, 122201.

[26] X. Cheng, C. Jouvaud, X. Ni, S. H. Mousavi, A. Z. Genack, A. B. Khanikaev, *Nature Mater.* **2016**, *15*, 542.

[27] N. Gao, S. Qu, L. Si, J. Wang, W. Chen, *Appl. Phys. Lett.* **2021**, *118*, 063502.

[28] W. Noh, H. Nasari, H.-M. Kim, Q. Le-Van, Z. Jia, C.-H. Huang, and B. Kanté, *Opt. Lett.* **2020**, 45, 4108-4111.

[29] Y. Gong, S. Wong, A. J. Bennett, D. L. Huffaker, S. S. Oh, *ACS Photonics* **2020**, 7, 2089.

[30] Y. Zeng, U. Chattopadhyay, B. Zhu, B. Qiang, J. Li, Y. Jin, L. Li, A. G. Davies, E. H. Linfield, B. Zhang, Y. Chong, Q. J. Wang, *Nature* **2020**, *578*, 246.

[31] A. M. Dubrovkin, U. Chattopadhyay, B. Qiang, O. Buchnev, Q. J. Wang, Y. Chong, N. I. Zheludev, *Appl. Phys. Lett.* **2020**, *116*, 191105.

[32] Q. Chen, L. Zhang, S. Xu, Z. Wang, E. Li, Y. Yang, H. Chen, *Appl. Phys. Lett.* **2020**, *116*, 231106.

[33] Q. Chen, L. Zhang, M. He, Z. Wang, X. Lin, F. Gao, Y. Yang, B. Zhang, H. Chen, *Adv. Optical Mater.* **2019**, *7*, 1900036.

[34] K. Kim, K. Om, *Adv. Optical Mater.* **2021**, *9*, 2001865.

[35] J. W. You, Q. Ma, Z. Lan, Q. Xiao, N. C. Panoiu, T. J. Cui, *Nat. Commun.* **2021**, *12*, 5468.

[36] X.-D Chen, X.-T He, J.-W Dong, *Laser Photonics Rev.* **2019**, *13*, 1900091.

[37] M. Goryachev, M. E. Tobar, *Phys. Rev. Applied* **2016**, *6*, 064006.

[38] M. I. Shalaev, S. Desnavi, W. Walasik, N. M. Litchinitser, *New J. Phys.* **2018**, *20*, 023040.

[39] Y. Yang, Z. Gao, H. Xue, L. Zhang, M. He, Z. Yang, R. Singh, Y. Chong, B. Zhang, H. Chen, *Nature* **2019**, *565*, 622.

[40] D. J. Bisharat, D. F. Sievenpiper, *Proc. SPIE* **2020**, *11290*, 112900N.

[41] J.-K. Yang, Y. Hwang, S. S. Oh, *Phys. Rev. Res.* **2021**, *3*, L022025.

[42] Q. Chen, L. Zhang, F. Chen, Q. Yan, R. Xi, H. Chen, Y. Yang, *ACS Photonics* **2021**, *8*, 1400.